AGU PUBLICATIONS

Geophysical Research Letters

RESEARCH LETTER
10.1002/2016GL068758

Special Section:
First results from NASA's Magnetospheric Multiscale (MMS) Mission

Magnetospheric Multiscale Mission observations and non-force free modeling of a flux transfer event immersed in a super-Alfvénic flow

C. J. Farrugia[1], B. Lavraud[2,3], R. B. Torbert[1], M. Argall[1], I. Kacem[2], W. Yu[1], L. Alm[1], J. Burch[4], C. T. Russell[5], J. Shuster[1], J. Dorelli[6], J. P. Eastwood[7], R. E. Ergun[8], S. Fuselier[4,9], D. Gershman[10], B. L. Giles[6], Y. V. Khotyaintsev[10], P. A. Lindqvist[10], H. Matsui[1], G. T. Marklund[10], T. D. Phan[11], K. Paulson[1], C. Pollock[6], and R. J. Strangeway[5]

[1]Space Science Center, University of New Hampshire, Durham, New Hampshire, USA, [2]Institut de Recherche en Astrophysique, Université de Toulouse, Toulouse, France, [3]Centre National de la Recherche Scientifique, Toulouse, France, [4]Southwest Research Institute, San Antonio, Texas, USA, [5]University of California, California, USA, [6]NASA Goddard Space Flight Center, Greenbelt, Maryland, USA, [7]The Blackett Laboratory, Imperial College London, London, UK, [8]University of Colorado Boulder, Boulder, Colorado, USA, [9]Space Science Department, University of Texas at San Antonio, San Antonio, Texas, USA, [10]Swedish Institute of Space Physics, Uppsala, Sweden, [11]Space Sciences Laboratory, Berkeley, California, USA

Key Points:
- Draping signatures around an FTE
- Non-force free modeling of the FTE flux rope
- Detailed plasma behavior in and around FTE

Supporting Information:
- Supporting Information S1

Correspondence to:
C. J. Farrugia,
charlie.farrugia@unh.edu

Citation:
Farrugia, C. J., et al. (2016), Magnetospheric Multiscale Mission observations and non-force free modeling of a flux transfer event immersed in a super-Alfvénic flow, *Geophys. Res. Lett.*, *43*, 6070–6077, doi:10.1002/2016GL068758.

Received 18 MAR 2016
Accepted 17 MAY 2016
Accepted article online 23 MAY 2016
Published online 30 JUN 2016

©2016. American Geophysical Union. All Rights Reserved.

Abstract We analyze plasma, magnetic field, and electric field data for a flux transfer event (FTE) to highlight improvements in our understanding of these transient reconnection signatures resulting from high-resolution data. The ~20 s long, reverse FTE, which occurred south of the geomagnetic equator near dusk, was immersed in super-Alfvénic flow. The field line twist is illustrated by the behavior of flows parallel/perpendicular to the magnetic field. Four-spacecraft timing and energetic particle pitch angle anisotropies indicate a flux rope (FR) connected to the Northern Hemisphere and moving southeast. The flow forces evidently overcame the magnetic tension. The high-speed flows inside the FR were different from those outside. The external flows were perpendicular to the field as expected for draping of the external field around the FR. Modeling the FR analytically, we adopt a non-force free approach since the current perpendicular to the field is nonzero. It reproduces many features of the observations.

1. Introduction

The major aim of the Magnetospheric Multiscale Mission (MMS) is to make observations in the diffusion regions (DRs) of reconnection sites, where energy is transferred from the magnetic field to the particles. DRs are spatially small structures but have large-scale consequences for magnetospheric dynamics. With scale sizes of a few tens of kilometers, a spacecraft can cross them in a few seconds. MMS was designed to provide multipoint, high time resolution data to accurately study DRs.

One aspect of the interaction of the magnetosphere with the solar wind is the transient form of reconnection occurring in short bursts and called flux transfer events (FTEs) [*Russell and Elphic*, 1978]. These may be isolated, i.e., have lost magnetic connection with the X line, or still active, so-called "crater" FTEs, where regions of the structure are still magnetically connected to the X line [*LaBelle et al.*, 1987; *Rijnbeek et al.*, 1987; *Farrugia et al.*, 1988, 2011]. Much has been learned about FTEs from the ISEE, Cluster, and Time History of Events and Macroscale Interactions (THEMIS) missions. How is high-resolution data going to improve on this?

(i) With four-spacecraft timing at very short time scales, we derive the motion of small structures relative to the spacecraft [*Russell et al.*, 1983]; (ii) we get a better handle on flows parallel/perpendicular to **B** even for events lasting a few seconds; (iii) we make detailed study of the draping of the ambient field around the FTE; (iv) we determine small-scale currents; and (v) we introduce electric field measurements in FTE analyses.

In this paper we focus on an FTE observed by MMS on 15 August 2015. We use data from the fluxgate magnetometers [*Russell et al.*, 2014] (resolution in burst mode = 128 Hz), Fast Plasma Investigation (FPI) [*Pollock et al.*, 2016] (resolution = 8 and 34 Hz for ions and electrons, respectively), Electron Drift Instrument (EDI) [*Torbert et al.*, 2014] (resolution = 1024 Hz in burst mode), and electric field [*Lindqvist et al.*, 2014] (resolution = 32 Hz). These are much higher than previously available, especially the plasma measurements.

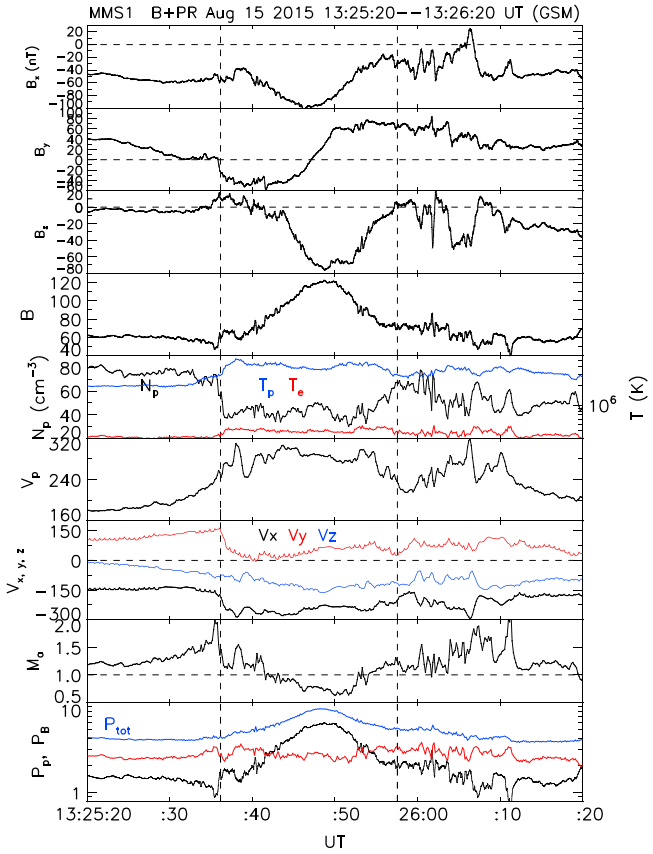

Figure 1. (first to ninth panels) Magnetic field components in GSM coordinates, total field strength, proton density and ion (blue) and electron (red) temperatures, bulk speed and GSM velocity components, Alfvén Mach number, and the pressures (black = magnetic; red = proton + electron, and blue = total pressure).

We target the following topics: (i) connectivity (North/South Hemisphere) and direction of motion; the former is derived independent of the polarity of the normal **B** component, which can be an ambiguous indicator [*Daly et al.*, 1984], (ii) observational effects of the draping of magnetic field lines around the FTE immersed in a super-Alfvénic flow, and (iii) non-force free modeling.

The layout of the paper is as follows. We present an overview figure of observations from MMS1. This brings out various features that we will discuss in the succeeding sections. We finish with a discussion.

2. Observations

Figure 1 shows an overview plot from MMS1 for the 1 min interval 13:25:20 to 13:26:20 UT, 15 August 2015. The spacecraft were approaching apogee, and MMS1 was located in the magnetosheath at (1.325, 9.159, −4.319) R_E (GSM; at start of the event). The geomagnetic latitude and local time were −20.7° and 16.5 h, respectively. The spacecraft separation was 150–200 km. The observations were made under very compressed magnetosphere conditions ($P_{dyn} \approx 11$ nPa) during the passage of an interplanetary coronal mass ejection. (Figure S1 in the supporting information.)

A clear FTE is observed in the interval bracketed by the two vertical guidelines. (i) A large rotation in **B**, with a bipolar variation in its *y* component. Given the location of MMS, the *y* direction may be taken as a rough proxy for the local magnetopause normal. The sign change of B_y at the start of the FTE (first vertical dashed line) will be used in four-spacecraft timing. The helicity of the underlying flux rope is left handed. (ii) There is a strong magnetic field which peaks at ∼120 nT near the B_y polarity change. The event lasts for ∼20 s and has a peak-to-peak B_y excursion ∼130 nT. It starts and ends in the magnetosheath. (iii) The negative-to-positive B_y variation indicates a reverse FTE. (iv) Inside the flux tube there is a drop in N_p and a concomitant rise in T_p and T_e, as expected for magnetosheath FTEs. (v) There are accelerated flows which start even before MMS1

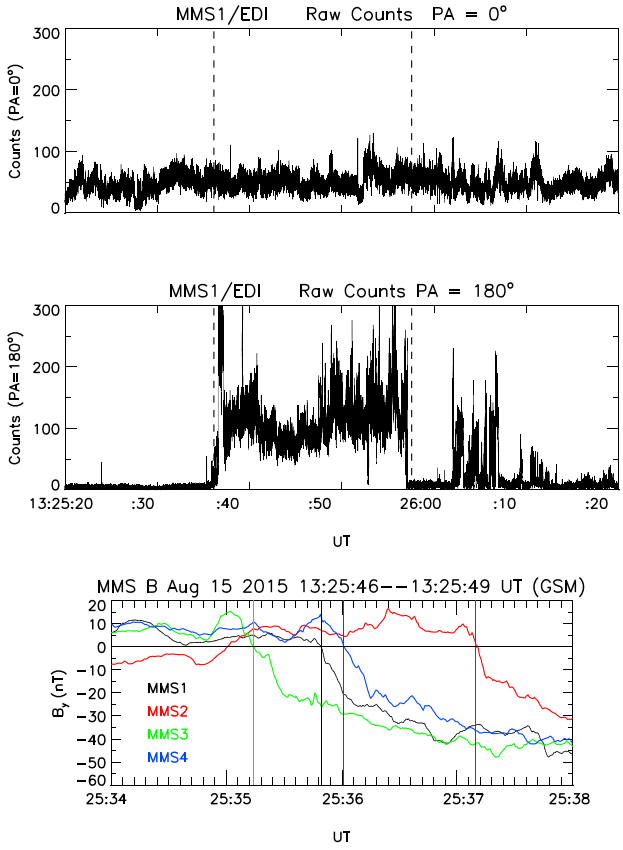

Figure 2. PA information of raw count rates of 500 eV electrons from EDI in burst mode. (top) PA = 0°. (middle) PA = 180°. See also supporting information Figure S3. (bottom) The arrival of the front boundary of the FTE at the various spacecraft.

enters the flux tube. (vi) The Alfvén Mach number *MA* shows that the ambient flow (say at 13:25:20 UT) is super-Alfvénic. (vii) The pressure profiles show a dominance of the magnetic pressure P_B around the center, but not near the edges.

2.1. Motion and Connectivity of the FTE

Reverse FTEs are typically connected to the Southern Hemisphere [*Rijnbeek et al.*, 1982]. The connectivity here is best seen through particle data. We use 500 eV electrons from EDI [*Torbert et al.*, 2014; *Burch et al.*, 2015]. Figure 2 shows a strong increase in the count rates at 180° pitch angle (PA). Now from Figure 1, the electron energy in the magnetosheath is approximately a few tens of eV. The electrons at EDI must, then, be coming from the magnetosphere, and their PA anisotropy indicates magnetic connection to the Northern Hemisphere. This inference is corroborated by FPI data, also showing consistent PA anisotropies of energetic electrons (962–2026 eV; supporting information Figure S2).

The direction of motion is inferred using four-spacecraft measurements [*Russell et al.*, 1983]. We determined the arrival time of the front boundary of the FTE (see Figure 2) and obtained a propagation velocity = 106.7 × (−0.09, 0.47, −0.88) km/s (GSM). Thus, we have an FTE connected to the Northern Hemisphere and moving southeast.

2.2. Plasma Flows in and Around the FTE

Inside the flux rope the magnetic field is twisted [*Cowley*, 1982; *Paschmann et al.*, 1982]. Data from past missions such as Cluster or THEMIS would have only 5 to 7 points inside the FTE. With the high-resolution MMS data, we can visualize the field twist rather nicely from the flows, as shown in Figure 3. The flow pattern inside the FTE reflects the two-component **B**-field (first–fourth panels). The axial **B** component is a minimum, and the azimuthal **B** component is a maximum, at the first outer boundary. Here $\mathbf{V}_\perp$ is maximum and $\mathbf{V}_\parallel$ is minimum. Axial **B** maximizes near the axis, where simultaneously azimuthal **B** is at a minimum. Here in turn, $\mathbf{V}_\parallel$ is a

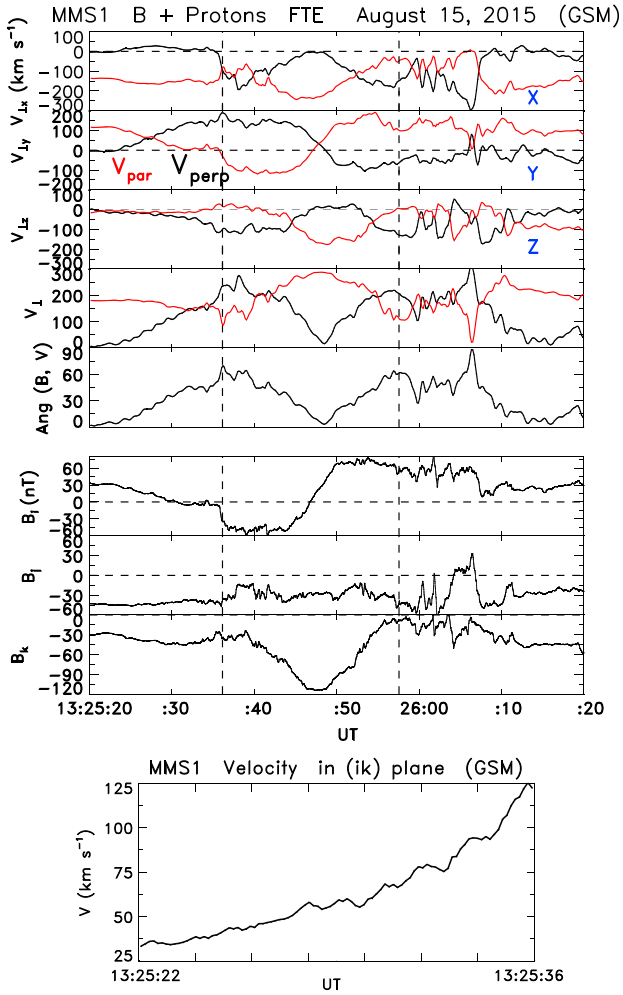

Figure 3. The proton velocities in field-aligned coordinates. (first to fourth panels) Red (black) traces refer to the parallel (perpendicular) components. (fifth panel) The angle between **B** and **V**. (sixth to eighth panels) The components of **B** in minimum variance coordinates **ijk**. (ninth panel) The plasma velocity in the *ik* plane, i.e., containing the FR axis (**k**) and perpendicular to the incoming flow velocity (**j**).

maximum and $\mathbf{V}_\perp = 0$. The presence of an azimuthal **B** component results in a quasisinusoidal and anticorrelated pattern in the perpendicular and parallel flows.

Accelerated flows are seen in the FTE. But there are also accelerated flows just outside it (Figure 1), and different components are accelerated or deflected. V_y and $|V_z|$ increase on approaching the FTE. $|V_x|$ is enhanced inside the tube, but not outside, while V_y is reduced inside. Outside the FTE and starting at 13:25:26 UT, the field-aligned flows in Figure 3 show a clear enhancement in the component perpendicular to the field but not in the parallel component (fourth and fifth panels). This is indicative of draping. In summary, we have two types of accelerated flows, due to different origins: reconnection inside and field line draping outside the flux rope.

2.3. Orientation of the Flux Rope Axes at the Various Probes

We performed a minimum variance analysis on high-resolution magnetic field data [*Sonnerup and Cahill*, 1967; *Sonnerup and Scheible*, 1998]. We find an exceptionally well-determined axis orientation, with the ratio of intermediate-to-minimum eigenvalues of 20 (MMS1), 24 (MMS2), 28 (MMS3), and 32 (MMS4) (supporting information Table S1). The axes are practically aligned with each other, the minimum angle being that between MMS1 and MMS3 (~0.3°) and the maximum between MMS2 and MM4 (~12.6°). Following *Goldstein* [1983] but in a different context, we note that in the (**ijk**) system employed here the axis (**k**) corresponds to the intermediate eigenvalue. The unit vector **j**, corresponding to the minimum eigenvalue, is oriented such that the largest field rotation takes place in the *ik* plane. Figure 3 (sixth to eighth panels) shows

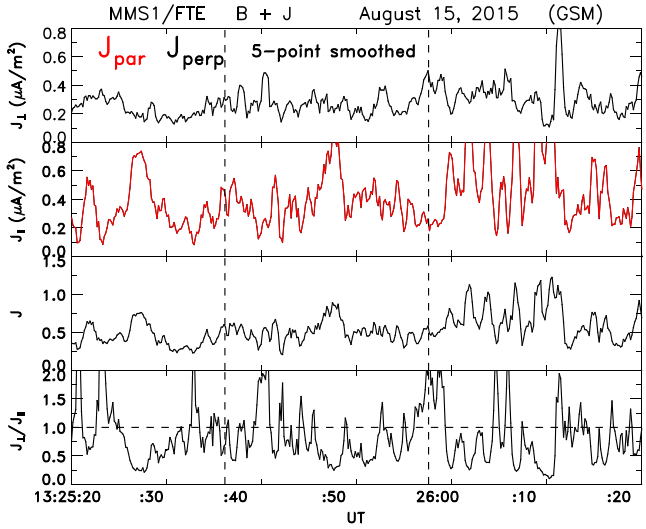

Figure 4. The current densities, determined from the FPI instrument for MMS1. (first to third panels) Perpendicular and parallel current densities are shown in black and red, respectively. (fourth panel) Ratio of current densities.

the result for MMS1. Almost perfect symmetry results (even more impressive at MMS3, Figure S3). The small but nonzero B_j, present at all spacecraft, indicates a spacecraft trajectory which does not pass through the axis. Taking this "impact parameter" to be zero, and using the propagation speed and a duration of 21.4 s, we estimate a flux tube radius of ~0.18 R_E.

We now discuss Figure 3 (ninth panel), showing the velocity in the *ik* plane. As it approaches the flux rope, the flow accelerates (from 40 to 125 km/s) while aligning itself parallel to the tube and perpendicular to **B**. The draping region (~13:25:26 to ~13:25:38 UT) is approximately one flux rope radius.

The spacecraft positions in the *LM* plane when the front boundary crosses are shown in Figure S4. Shown in orange is the projection of the propagation velocity derived above. The magnetopause plane (LM) is viewed from the Sun. Since there were no magnetopause crossings close enough to obtain the normal to the magnetopause from a cross product or a minimum variance analysis of the field or currents, we derived this from the *Shue et al.* [1998] model (supporting information Figure S5). At 13:25 UT, $N = (0.61, 0.72, -0.34)$, i.e., with a major component along GSM Y, but also pointing south, consistent with the position of MMS.

2.4. Analytical Modeling of the FTE Flux Rope

Figure 1 (ninth panel) shows that the plasma β rises above unity near the edges of the event. This questions the validity of using force free modeling ($\mathbf{j} \times \mathbf{B} = 0$) here. Thanks to high-resolution MMS measurements, we now derive a direct confirmation of this from the current densities.

In force free conditions, $\mathbf{j}_\perp = 0$. In Figure 4 we show the current densities for MMS1 as derived from FPI data. $\mathbf{J} = n_e q(\mathbf{V_i} - \mathbf{V_e})$, where n_e is the electron density, q is the electron charge, and V_i and V_e are the velocities of the protons and electrons, respectively. We plot the five-point-smoothed perpendicular (black) and parallel velocities. Figure 4 (first and fourth panels) shows that $\mathbf{J}_\perp$ is generally not zero for this FTE. For analytical modeling of the flux tube we shall thus use a non-force free model.

Specifically, we apply that of *Hidalgo et al.* [2002]. In this model, the tube cross section is taken to be circular. Current densities are assumed to be constant, with the radial component = 0. From Maxwell's equations, it is found that the poloidal (azimuthal, ϕ) component of the magnetic field results from the toroidal component of the current density ($B_\phi = (\mu_0/2) j_k r$), and the toroidal (axial, k) field component is due to the poloidal component of the current density ($B_k = \mu_0 j_\phi (R - r)$. Here R is the tube radius and r gives the position of the spacecraft inside the flux tube.

We then carry out a least squares fit. We do not assume an axis orientation. The flux tube's magnetic field is sampled along the spacecraft trajectory at spatial intervals given by the z component (main one) of the propagation velocity multiplied by the time. Figure 5 shows the fitted curves in various colors and the data (dotted) for all four spacecraft. The fits are fairly good. The derived J's range from 2.1 μA/m^2 (MMS1) to 2.8 μA/m^2

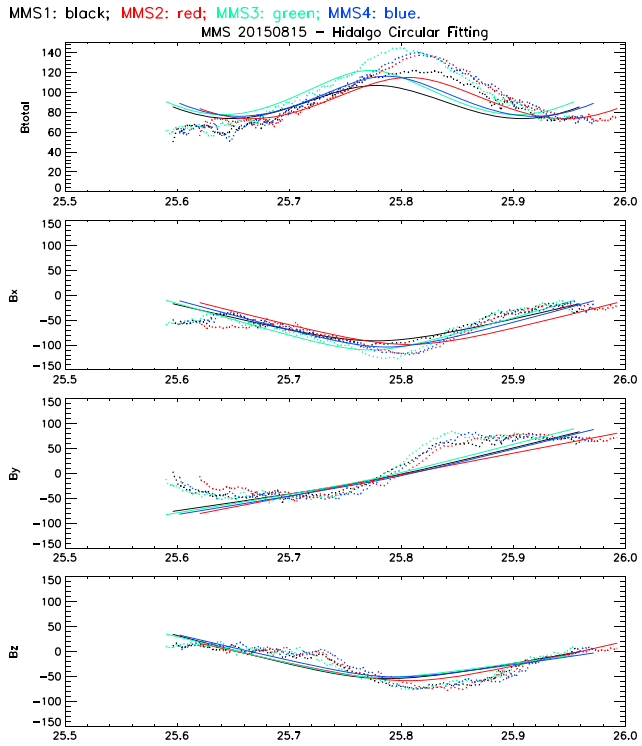

Figure 5. Fits to the Hidalgo model (see text for details). The data from the various spacecraft are shown with colored dots (legend at the top). The fits are shown by colored line traces.

(MMS3), i.e., within a factor of 2 of the values obtained from FPI data. The impact parameters lie in the range 0.19 *R* (MMS3) and 0.28 *R* (MMS1), consistent with the strength of the magnetic field seen at the various spacecraft (supporting information Table S2). The flux tube radius *R* is calculated as ~0.14 R_E. The orientations of the axis at the various spacecraft are within a few degrees from those determined by minimum variance.

3. Discussion

The aim of this paper is to show how high-resolution magnetic field, electric field, and plasma data acquired by four closely spaced spacecraft can add to our knowledge of FTEs, a staple in reconnection processes at the magnetopause. The event was observed near dusk at low geomagnetic latitudes. It occurred during passage of the rear end of a 5.5 h long span of high dynamic pressure on 15 August 2015 during the passage of an ICME. We now elaborate on some points arising from the data analysis.

In the absence of more accurate data-based methods, we used the *Shue et al.* [1998] magnetopause to obtain the magnetopause normal. This model was derived for extreme interplanetary B_z and P_{dyn} conditions, so it is appropriate here since both relevant parameters were high (−8 nT and −11 nPa, respectively). Soon after the event the pressure fluctuated while dropping to lower values and this hindered a robust identification of a magnetopause crossing.

The FTE was a reverse FTE, which is usually connected to the Southern Hemisphere [*Rijnbeek et al.*, 1982]. The anisotropies of particle data from EDI and FPI showed, instead, a topological connection to the Northern Hemisphere. Four-spacecraft timing gave a propagation velocity in a southeast direction. Such a situation is rare, but not unknown. FTEs moving north and connected to the Southern Hemisphere were, for example, discussed by *Daly et al.* [1984]. The balance of forces is central. In our case, the (southward) forces exerted by the ambient flow have to exceed those due to (northward) magnetic tension in the bent flux tube, which are released at a speed less than the Alfvén speed. This is satisfied if the external flow is super-Alfvénic, which is the case here (Figure 1). The important issue as to where the X line(s) was/were with respect to the spacecraft is reserved for a future study.

In our analysis we followed the "isolated flux rope" paradigm [*Russell and Elphic*, 1978]. We checked that $\mathbf{E} + \mathbf{V} \times \mathbf{B} = 0$, so this is a valid assumption. (Supporting information Figure S6.)

The flow behavior was particularly interesting. We documented two types of accelerated flows, affecting different components: reconnection (inside the flux rope) and draping of the field external to the flux rope, focusing on the latter. We gave what we believe are the first observations on draping-related accelerated flows around an FTE-FR immersed in a compressible flow. The draped field exerts a $\mathbf{J} \times \mathbf{B}$ force, which accelerates the plasma perpendicular, but not parallel, to the magnetic field. This accelerated flow was furthermore shown to be aligned parallel to the FR, i.e., in the (*ik*) plane. The width of the draping region was about the FR radius.

The situation has an analog in the draping pattern near the magnetopause. Draping of the magnetosheath field around the magnetopause has been addressed in various studies [*Chen et al.*, 1993; *Farrugia et al.*, 1998; *Rosenqvist et al.*, 2007; *Lavraud et al.*, 2007; *Lavraud and Borovsky*, 2008; *Erkaev et al.*, 2011, 2012; *Harris et al.*, 2013]. One major result is that as a result of the magnetic tension and pressure, the magnetosheath flow near the magnetopause is accelerated in a direction perpendicular to the magnetic field. In such studies an enhancement of the magnetosheath flow velocity in a direction perpendicular to $\mathbf{B}$ is taken as irrevocable proof of draping. Finally, we note that we directed our attention to the magnetosheath region near the front boundary of the FTE. Near its rear boundary, complex processes are likely taking place (Figure 1). Understanding these is subject of future work.

Another novel aspect is the non-force free fitting of the FTE FR in a terrestrial context. In a few previous attempts researchers have used linear force-free fitting [*Lundquist*, 1950]. This may sometimes be appropriate [see *Zhang et al.*, 2008], but not in this case because $\mathbf{J}_\perp$ is nonzero. We showed results from one such model. The general agreement with observations motivates the future use of other non-force free models, possibly ones with fewer assumptions. For completeness, we also compared the results with those obtained from linear force free fitting. We found that the normalized goodness-of-fit parameter (χ^2) is comparable to, but not better than, that obtained in the force-free case. This again stresses the need of trying other non-force free models.

Acknowledgments
We would like to express our gratitude to all MMS teams for making this exciting mission possible. We thank Steve Petrinec and Karl-Heinz Trattner for useful discussions. This work was supported by the MMS grant NNG04EB99C and Wind grant. IRAP contribution to MMS was supported by CNES. The data we used are from the LASP and UNH MMS data centers.

References

Burch, J. L., T. E. Moore, R. B. Torbert, and B. L. Giles (2015), Magnetospheric multiscale overview and science objectives, *Space Sci. Rev.*, *199*, 5–21, doi:10.1007/s11214-015-0164-9.

Chen, S.-H., M. G. Kivelson, J. T. Gosling, R. J. Walker, and A. J. Lazarus (1993), Anomalous aspects of magnetosheath flow and of the shape and oscillations of the magnetopause during an interval of strongly northward interplanetary magnetic field, *J. Geophys. Res.*, *98*, 5727–5742.

Cowley, S. W. H. (1982), The causes of convection in the Earth's magnetosphere: A review of developments during the IMS, *Rev. Geophys.*, *20*, 531–565.

Daly, P. W., M. A. Saunders, R. P. Rijnbeek, N. Sckopke, and C. T. Russell (1984), The distribution of reconnection geometry in flux transfer events using energetic ion, plasma and magnetic data, *J. Geophys. Res.*, *89*(A6), 3843–3854, doi:10.1029/JA089iA06p03843.

Erkaev, N. V., C. J. Farrugia, B. Harris, and H. K. Biernat (2011), On accelerated magnetosheath flows under northward IMF, *Geophys. Res. Lett.*, *38*, L01104, doi:10.1029/2010GL045998.

Erkaev, N. V., C. J. Farrugia, A. V. Mezentsev, R. B. Torbert, and H. K. Biernat (2012), Accelerated magnetosheath flows caused by IMF draping: Dependence on latitude, *Geophys. Res. Lett.*, *39*, L01103, doi:10.1029/2011GL050209.

Farrugia, C., R. Rijnbeek, M. Saunders, D. Southwood, D. Rodgers, M. Smith, C. Chaloner, D. Hall, P. Christiansen, and L. Woolliscroft (1988), A multi-instrument study of flux transfer event structure, *J. Geophys. Res.*, *93*, 14,465–14,477.

Farrugia, C. J., H. K. Biernat, N. V. Erkaev, L. M. Kistler, G. Le, and C. T. Russell (1998), MHD model of magnetosheath flow: Comparison with AMPTE/IRM observations on 24 October, 1985, *Ann. Geophys.*, *16*, 518–527.

Farrugia, C. J., et al. (2011), "Crater" flux transfer events: Highroad to the X line?, *J. Geophys. Res.*, *116*, A02204, doi:10.1029/2010JA015495.

Goldstein, H. (1983), On the field configuration in magnetic clouds, in *Solar Wind Five*, pp. 731–733, NASA Conf. Publ., CP-2280, Germany.

Harris, B., C. J. Farrugia, N. V. Erkaev, and R. B. Torbert (2013), Observational aspects of IMF draping-related magnetosheath accelerations for northward IMF, *Ann. Geophys.*, *31*, 1779–1789.

Hidalgo, M. A., C. Cid, A. F. Vinas, and J. Sequeiros (2002), A non-force-free approach to the topology of magnetic clouds in the solar wind, *J. Geophys. Res.*, *107*(1), 1002, doi:10.1029/2001JA900100.

LaBelle, J., R. Treumann, G. Haerendel, O. Bauer, G. Paschmann, W. Baumjohann, H. Lühr, R. Anderson, H. Koons, and R. Holzworth (1987), AMPTE IRM observations of waves associated with flux transfer events in the magnetosphere, *J. Geophys. Res.*, *92*, 5827–5843.

Lavraud, B., J. E. Borovsky, A. J. Ridley, E. W. Pogue, M. F. Thomsen, H. Réme, A. N. Fazakerley, and E. A. Lucek (2007), Strong bulk plasma acceleration in Earth's magnetosheath: A magnetic slingshot effect?, *Geophys. Res. Lett.*, *34*, L14102, doi:10.1029/2007GL030024.

Lavraud, B., and J. E. Borovsky (2008), Altered solar wind-magnetosphere interaction at low Mach numbers: Coronal mass ejections, *J. of Geophys. Res.*, *113*, A00B08, doi:10.1029/2008JA013192.

Lindqvist, P.-A., et al. (2014), The spin-plane double-probe electric field instrument for MMS, *Space Sci. Rev.*, *199*, 137–165, doi:10.1007/s11214-014-0116-9.

Lundquist, S. (1950), Magnetohydrostatic fields, *Ark. Fys.*, *2*, 361.

Paschmann, G., G. Haerendel, I. Papamastorakis, N. Sckopke, S. J. Bame, J. T. Gosling, and C. T. Russell (1982), Plasma and magnetic field characteristics of magnetic flux transfer events, *J. Geophys. Res.*, *97*, 2159–2168.

Pollock, C., et al. (2016), Fast plasma investigation for magnetosphere multiscale, *Space Sci. Rev.*, *199*, 331–406, doi:10.1007/s11214-016-0245-4.

Rijnbeek, R. P., S. W. H. Cowley, D. J. Southwood, and C. T. Russell (1982), Observations of reverse polarity flux transfer events at the Earth's dayside magnetopause, *Nature*, *300*, 23–26, doi:10.1038/300023a0.

Rijnbeek, R. P., C. J. Farrugia, D. J. Southwood, M. W. Dunlop, W. A. C. Mier-Jedrzejowicz, C. P. Chaloner, D. S. Hall, and M. F. Smith (1987), A magnetic boundary signature within flux transfer events, *Planet. Space Sci.*, *35*, 871–878.

Rosenqvist, L., A. Kullen, and S. Buchert (2007), An unusual giant spiral arc in the polar cap region during the northward phase of a Coronal Mass Ejection, *Ann. Geophys.*, *25*, 507–517.

Russell, C. T., and R. C. Elphic (1978), Initial ISEE magnetometer results: Magnetopause observations, *Space Sci. Rev.*, *22*, 681–715.

Russell, C. T., M. Mellott, E. J. Smith, and J. H. King (1983), Observations of interplanetary shocks: Four spacecraft determination of shock normals, *J. Geophys. Res.*, *88*(A6), 4739–4748.

Russell, C. T., et al. (2014), The magnetospheric multiscale magnetometers, *Space Sci. Rev.*, *199*, 189–256, doi:10.1007/sl1214-014-0057-3.

Shue, J.-H., et al. (1998), Magnetopause location under extreme solar wind conditions, *J. Geophys. Res.*, *103*(A8), 17,691–17,700.

Sonnerup, B. U. Ö., and L. J. Cahill (1967), Magnetopause structure and attitude from Explorer 12 observations, *J. Geophys. Res.*, *72*, 171–183.

Sonnerup, B. U. Ö., and M. Scheible (1998), Minimum and maximum variance analysis, in *Analysis Methods for Multi-Spacecraft Data*, edited by G. Paschmann and P. W. Daly, p. 1850, ESA Publ., Noordwijk, Netherlands.

Torbert, R. B., et al. (2014), The FIELDS instrument suite on MMS: Scientific objectives, measurements, and data products, *Space Sci. Rev.*, *199*, 105–135, doi:10.1007/s11214-014-0109-8.

Zhang, H., K. K. Khurana, M. G. Kivelson, V. Angelopoulos, Z. Y. Pu, Q.-G. Zong, J. Liu, and X.-Z. Zhou (2008), Modeling a force-free flux transfer event probed by multiple Time History of Events and Macroscale Interactions during Substorms (THEMIS) spacecraft, *J. Geophys. Res.*, *113*, A00C05, doi:10.1029/2008JA013451.